

Strengthening Effects of Tool-Mounted Ultrasonic Vibrations during Friction Stir Lap Welding of Al and Mg Alloys



SACHIN KUMAR and CHUANSONG WU

Ultrasonic assistance in friction stir welding of dissimilar metals has proven efficacious in suppressing intermetallics and enhancing joint quality. In a quest to multiply the ultrasonic effects, a tool-mounted ultrasonic vibration system is used to characterize the welds. The ultrasonic vibrations are enforced in the stirred zone (SZ) along the welding direction. Widely used and industrially applicable AA6061-T6 and AZ31B Mg alloys are taken for experimentation in this study. For a better and in-depth interpretation of ultrasonic effects, weld microstructure characterization is done for various parameters and at different regions of interest. The outcomes suggest the efficacy of acoustic assistance to effectively induce enhanced material turbulence in the SZ and, thus, permit intense intermixing of Al and Mg. The X-ray diffraction and microhardness results diminished β -Al₃Mg₂ and γ -Al₁₂Mg₁₇ intermetallic compound (IMC) phases and improved weld quality for acoustic joints. Unlike previous studies, the electron backscatter diffraction analysis is added to visualize IMC fragmentation and elimination of the β phase in the ultrasonically treated weld zone. The localized fracture scan of ultrasonic welds resembles deep dimples, signifying a mixed mode of failure.

<https://doi.org/10.1007/s11661-021-06282-w>

© The Minerals, Metals & Materials Society and ASM International 2021

I. INTRODUCTION

ALUMINUM (Al) and magnesium (Mg) alloys are important structural metals and are used extensively in numerous aerospace and automobile applications.^[1] To have better design flexibility for their widespread applications, a successful joining of Al and Mg is essential.^[2] Various fusion welding processes have been attempted in the past; however, they have proven unattractive due to the presence of massive intermetallic compounds (IMCs), weldment defects, coarser grains, and loss of strength.^[2] Thus, the primary technical challenge to join Mg and Al alloys for structural applications is to develop a successful joining method.

Recently, a solid-state joining technique known as friction stir welding (FSW) was attempted and was found effective in obtaining high strength joints.^[3–5] Due to the comparatively lower heat input, high strain rate, and intense plastic deformation,^[6–9] the friction-stir-welded joints claim narrow IMC layers and better joint quality.^[10,11] The structural components made with the friction-stir-welded Al and Mg alloys can

be used in a wide variety of industrial applications such as in aircraft and defense, electrical generator housing, automotive, car chassis, and military helicopters.^[2]

Though during the FSW of dissimilar alloys the IMCs are reduced, their presence is unavoidable. Typically, Al₁₂Mg₁₇ and Al₃Mg₂ IMC phases are found to coexist across the dissimilar interfaces of Al and Mg alloy joints.^[12,13] The formation of IMCs is a serious concern because they promote liquation cracking across the weld sections and severely deteriorate the weld quality. Venkateswaran *et al.*^[14] and Dorbane *et al.*^[15] reported poor strength of dissimilar Al/Mg joints due to enormous IMCs and brittle failure. Chen and Nakata^[16] confirmed eutectic (γ -Mg) and dendritic (γ -Al₁₂Mg₁₇) formation in the stirred zone (SZ), signifying the solidification structure and constitutional liquation. Kostka *et al.*^[17] observed that a thorough elimination of IMCs was quite challenging; however, a notable reduction in their thicknesses could be feasible.

During the FSW of dissimilar alloys, some material is chipped off from their faying surfaces and gets intermixed in the SZ. Its massive accumulation permits the nucleation of parallel layer intercalated structures and corresponds to interdiffusion.^[18] When the SZ temperature is about 437 °C, a small volume of material gets liquefied much below the melting temperatures of the respective metal. It is known as constitutional liquation.^[12] It favors the rapid growth of IMC phases across the dissimilar interfaces. Typically, the IMC phases are

SACHIN KUMAR and CHUANSONG WU are with the MOE Key Lab for Liquid-Solid Structure Evolution and Materials Processing, Institute of Materials Joining, Shandong University, Jinan, 250061 P.R. China. Contact email: wucs@sdu.edu.cn

Manuscript submitted September 28, 2020; accepted April 5, 2021.

Article published online May 10, 2021

substantially fragile, brittle, and responsible for reducing the weld strength.^[16,19] The IMC growth can be limited by reducing the heat addition by performing FSW at lower rotation speeds. In this situation, the interfaces may lack adequate plasticization and result in poor material mixing. All together they may contribute to weld defects and reduced joint strength.^[20]

Notable attempts have been made to improve the weldment strength by reducing the IMC formation. For example, Mofid *et al.* reported a considerable thinning of IMC layers by adding nitrogen gas with the FSW process.^[21] During stationary shoulder FSW of Al-Mg alloys, Ji *et al.*^[22] observed reduced IMCs and improved weld strength.

The ultrasonic addition in the FSW process has gained worldwide acceptance for obtaining better quality joints of Al^[23–26] and Mg alloys.^[27–29] A significant reduction in IMC layer thickness and improvement in weld strength were observed in the joints made with ultrasonic addition.^[28,30,31] Liu *et al.*^[32] found a marginal rise in the weld strength and interlocking features during the ultrasonic addition. Strass *et al.* reported fragmentation of IMCs and subsequent thickness reduction due to ultrasonic addition.^[33] A rise in weldment strength with acoustic assistance is explained due to the alteration of bi IMC layers into the monolayer. Lv *et al.*^[28] added ultrasonic vibration ahead of the welding tool pin and reported an improvement in Al-Mg alloy weld strength with a notable reduction in IMC thickness.

The ultrasonic vibrations are a localized source of energy that get absorbed in the material's vacancies, dislocations, and grain boundaries in a very narrow zone close to the point of application.^[34,35] When ultrasonic addition in the FSW process is made at a distance from the SZ^[36] (placing the probe on top of the workpiece either leading or behind the tool at a certain distance), some percentage of its energy is lost in the time gap from ultrasonic probe contact and actual FSW. Consequently, the SZ does not or partly receives the acoustic energy and may cause insignificant effects on weld microstructure and mechanical properties. Hence, the weldment properties may be compromised. On the other hand, if acoustic assistance is made as close as possible to the SZ (as used in the current article), a major part of it will be absorbed in the SZ. It will result in better material mixing and fewer weld defects and a less significant rise in the weldment properties. Therefore, the ultrasonic energy needs to be dissipated in the localized region of interest to gain its maximum benefits. For the configuration used by Shi *et al.*,^[36] the continuous contact of a horn probe with the workpiece may produce friction and wear the horn material, which may alter the working frequency and amplitude. However, in the present configuration (as used in the current article), the frictional contact between the tool and horn tip is avoided using roller bearings.

In the present work, the authors developed a tool-mounted ultrasonic-assisted friction stir lap welding (U-FSLW) system, an upgrade of the older methods used by Park *et al.*^[37] and Kumar.^[38] The upgraded version of an ultrasonic system is comprised of noble

horn attachments that facilitate inducing a thermo-mechanical-acoustic effect into the SZ. Such a peculiarly designed ultrasonic vibration system has a specially developed ultrasonic horn, transducer, generator, and front attachments to ensure reliable contact with a specially designed rotating FSW tool. The horn axis is kept perpendicular to that of the FSW tool such that ultrasonic vibrations can be transferred along the welding direction into the weldment zone. The amplitude of ultrasonic vibration at the location of the tool shoulder is measured using a laser vibrometer, which comes out to $\sim 32 \mu\text{m}$. A detailed analysis of amplitude measurement is documented elsewhere.^[39] Preliminary work on such an ultrasonic system was done previously, aiming to visualize the acoustic effects on welding load, tool torque, power input, and mechanical and macrostructural characteristics of Al-Mg alloy joints.^[29]

It was reported that the recently developed ultrasonic system can effectively reduce the welding load and input power and improve the weldment strength.^[29,40] The reason is ascribed to intense material mixing, enhanced material flow, and a notable reduction in the IMC concentration during acoustic addition.^[29] A significant decrease of IMC layer thickness and improvement in weld quality by using a tool-mounted ultrasonic system was reported by Kumar *et al.*^[40,41] during the FSW of Al and Mg alloys. However, this study was focused on the butt configuration only.

To obtain an in-depth interpretation of ultrasonic effects on the process mechanism involved during microstructure characterization and fracture behavior of friction stir lap welding (FSLW) joints, a detailed analysis at different weld locations is vital. The authors were surprised to see that the past literature reported in this context is too scarce; in the case of a tool-mounted ultrasonic system, no such study (except Reference 29—which, however, lacks detailed microstructure and fracture analysis) is available that can quantify the effects of a tool-mounted ultrasonic on the microstructure and fracture behavior in detail for lap configuration of the joint. Therefore, to fill this critical literature gap, authors have portrayed a detailed fracture and microstructure characterization of conventional and ultrasonic joints at different regions of interest, which is further backed by a number of testing procedures. The electron backscatter diffraction (EBSD) based quantification of IMC phases is reported for the first time, which multiplies the novelty of this work.

II. EXPERIMENTAL PROCEDURE

An ultrasonic vibration assembly is designed, fabricated, and rigidly fixed with the FSLW machine using simple linkages. It is entailed to work under 3 kW power, $\sim 20,000$ Hz frequency, and $\sim 25 \mu\text{m}$ amplitude during the welding. A detailed schematic is shown in Figure 1. The ultrasonic vibrations can be transmitted to the Al/Mg lapped surfaces along the welding direction *via* a specially designed FSLW tool and through the horn front part.^[39] Further details about the ultrasonic system can be taken from the authors' previous work.^[39]

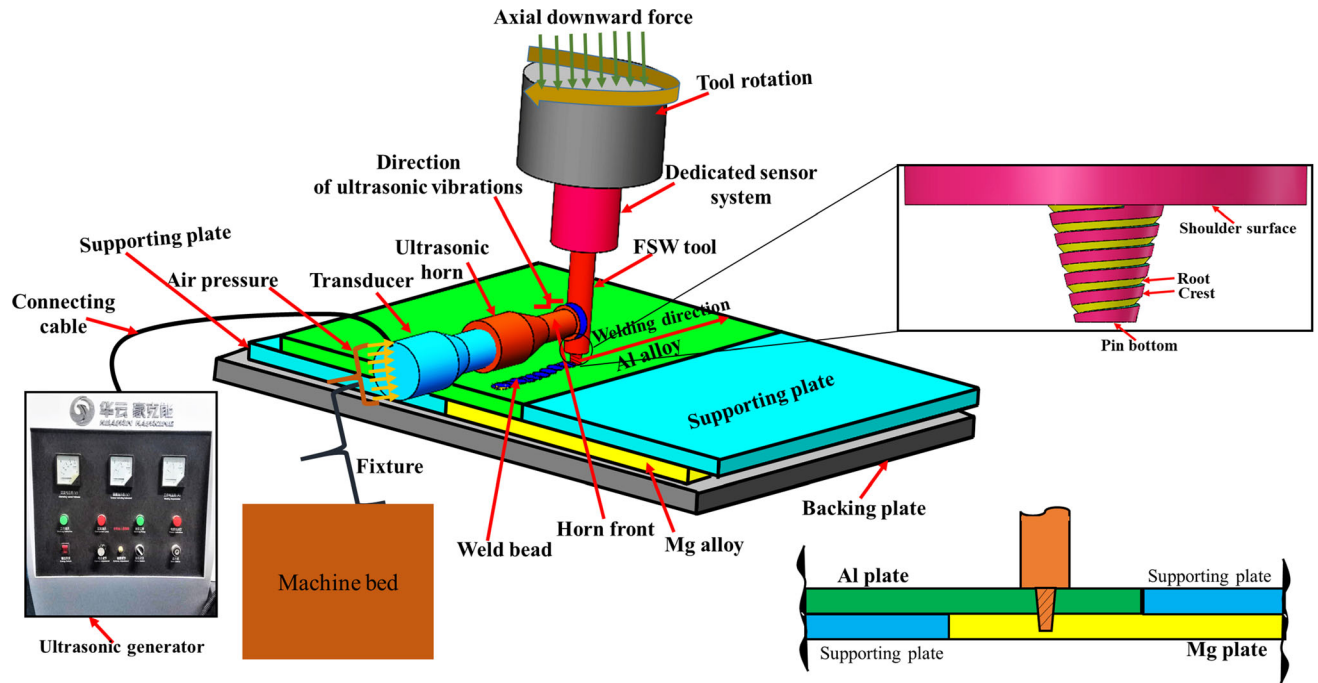


Fig. 1—(a) and (b) Schematic of the FSLW process and ultrasonic vibration assembly.

Table I. Chemical Composition of AA6061-T6 and AZ31B Mg Alloy^[29]

Alloy	Al	Zn	Mg	Mn	Si	Cu	Cr	Fe	Ti	Ca	C
AA6061-T6	bal.	0.05	0.82	0.05	0.75	0.28	0.01	0.06	0.03	0.01	3.1
AZ31B Mg alloy	2.5	0.5	bal.	0.15	0.1	0.05	0.15	0.3	0.02	0.05	2.63

The AA6061-T6 and AZ31B Mg alloy plates of thickness 3 mm each are taken to obtain dissimilar FSLW and U-FSLW joints. The nominal compositions of AA6061-T6 and AZ31B Mg alloy are listed in Table I. The plates of dimensions $300 \times 80 \text{ mm}^2$ are cut from bulk sheet volume such that the maximum plate dimension coincides with that of the rolling direction. The surfaces of cutout plates are deburred carefully to prevent any prior inhomogeneity. The specifications of the FSLW tool are presented in Table II. An overlap length of 30 mm is selected to obtain FSLW and U-FSLW joints, while the optimum parameters used in the current study are taken from the authors' previous work.^[29] The weld joints are numbered according to the mode of application and the parameters used, as shown in Table III.

The FSLW and U-FSLW welds are sectioned perpendicular to the weld direction, *i.e.*, in the plane of the weld cross sections. The samples are polished using different sets of emery papers of 600 to 3000 grit, followed by diamond slurry and colloidal silica as the polishing medium. The Mg and Al sides of the weld samples are etched using 1 mL HNO_3 + 1 mL CH_3COOH + 1 g $\text{H}_2\text{C}_2\text{O}_4$ + 150 mL distilled water and 2 mL HF + 5 mL HNO_3 + 95 mL distilled water,

respectively. A Zeiss daheng invasion camera microscope and JSM-6610 scanning electron microscope (SEM) equipped with energy dispersive X-ray spectrometry (EDS) capability were used to characterize the weld sections. A solution of $\text{HClO}_4:\text{C}_2\text{H}_5\text{OH} = 1:9$ at voltage 20 V is prepared to electropolish the samples for EBSD analysis. The EDAX-TSL OIM system mounted on a field emission SEM (Hitachi SU5000, 700F, 30 kV) is used to interpret the EBSD samples. Data cleanup using OIM EBSD software is carried out to map the fine microstructure. The phase analysis of the IMC region is done using a multifunctional DMAX-2500PC X-ray diffractometer (XRD). For tensile shear testing, FSLW and U-FSLW samples are cut transverse to the welding direction per ASTM E8/E8M standards.^[42] A Sans Yyl-20 universal testing machine working on a displacement control mode with a constant crosshead speed of 1 mm/min is used for tensile testing at room temperature [296.15 K (23 °C)]. The details of the tensile test samples have been reported in the previous study.^[29] At least three repetitions are made under each set of parameters, and their average values are taken for further analysis. The microhardness measurement is carried out at different weld depths using a hardness indentation

machine (UHL VMHT 001) at 200 gmf and 15-second dwell time.

III. RESULTS AND DISCUSSION

A. Optical Microscopic Investigations

Figures 2 through 7 show the macro- and microstructure of welds W#1 through W#6. Various regions of interest are taken into account (Figures 2(a) to 7(a)) and correspondingly shown in higher magnifications (Figures 2(b) to (e), 3(b) to (e), 4(b) to (i), 5(b) to (i), 6(b) to (e), and 7(b) to (e)). Irrespective of the parameters used, both metals are intermixed in the weld region. However, the intensity of intermixing is largely dependent on the tool rotation speed and acoustic assistance. Both the alloys cross their lapped interfaces to promote stirring (Figures 2(e), 3(d) and Figures 6(b), 7(d)), as the tool pin penetrates the Mg plate. The material flow in welds W#1, W#3, and W#5 illustrates minor traces of spiral material flow, which is primarily governed by the stirring action of the tool pin. The acoustic addition is observed to intensify the material movement in the SZ and assists in acquiring a well-defined bowl shape morphology (W#2, W#4, and W#6). Simultaneously, the SZs of the joints made with ultrasonic assistance have a deeper vortex compared to their counterparts (W#3 and W#4). An improvement in the material flow pattern during ultrasonic assistance can be attributable to the reduction in material viscosity and flow stresses, as theorized by Shi *et al.*^[36]

A number of spirals of material flow starting from top to bottom and vice versa can be seen in the SZ of the U-FSLW joint (W#4 in Figures 5(a), (f), and (g)). Such a material behavior can be expected because of stirring action intensified by tool rotation and ultrasonic effects.^[43] An improved material flow across the SZ due to ultrasonic addition can suppress the possible defects^[28,43] and enhance the bowl-shaped morphology and material interlocking.^[29] Adjacent to the dissimilar metal interfaces, the acoustic energy can accelerate the localized material plasticization and induce supplementary strain, easing the solid-state diffusion from one side to another in the metal matrix.^[44] All together it can effectively tighten the metal gripping and improve the weld strength.^[29] The formation of weld hook morphology and the IMC traces can be easily observed in the macrographs (Figures 2(a) to 7(a)) and the corresponding images in higher magnification (Figures 2(b) to (e), 3(b) to (e), 4(b) to (i), 5(b) to (i), 6(b) to (e), and 7(b) to (e)).

In the FSLW process, the faying regions of both the metals are perpendicular with respect to the FSW tool, making it cumbersome to break the oxide layer compared to the butt joints.^[45] Therefore, the interfacial regions away from the tool pin periphery do not get enough stirring and weld defects are formed. Besides, during lap welding, the pin penetrates the bottom metal for a certain amount of predefined depth to make a bonding region.^[45] It causes the top metal sheet interface to extrude at both sides to a certain level in the SZ^[45]

(Figure 4(a)). The material in the TMAZ region is also compelled to move upward owing to the vertical movement of the SZ material. As a result, a hook-shaped morphology has appeared across the lapped regions of both the metals (Figures 2(a) to 7(a)). The U-FSLW joint interfaces show more prominent interlocking compared to the conventional joints (such as in Figure 4(a)), which are due to the deep intermixing of Al and Mg alloys across the SZ (W#4 and W#6). Per Wei *et al.*,^[46] a flamelike interlocking across the dissimilar alloy's lap joints in the bonding regions can be considered beneficial to improve the joint strength.

The interlocking in U-FSLW joints is relatively more protruding due to the sharp clamping strips and hooking effects. The beneficial interlocking feature in the U-FSLW joints can be credited to the enhanced material flow and SZ turbulence caused by acoustic assistance.^[24,25,28] It is important to note that the massive intermixing of both the metals can also initiate the interdiffusion between Al-Mg substrates and can promote intermetallics. Per Yamamoto *et al.*,^[19] the discontinuous IMCs and their strips in the interlocking region can improve the joint strength, while a thick and coherent IMC layer may deteriorate the same. In most cases, irrespective of the parameters and the mode of application, the weld interfaces clearly show IMCs together with Al-Mg substrates (Figures 2(c), 2(d), 3(b), 4(b), 5(b), 5(h), 6(d), and 7(d)).

The EDS analysis of IMC regions (the EDS composition is not shown here) confirms Al_3Mg_2 (complex cubic β) and $\text{Al}_{12}\text{Mg}_{17}$ (cubic of α -Mn type γ) IMC phases. The same has been marked in Figures 2 through 7. In the Al-Mg binary system, the IMCs are formed due to the eutectics, $\text{Mg} + \text{Al}_{12}\text{Mg}_{17}$ (57 pct Mg) at 437 °C and $\text{Al} + \text{Al}_3\text{Mg}_2$ (37 pct Mg) at 450 °C.^[12,47] Yamamoto *et al.*^[19] stated that the maximum temperature in the FSLW process was below the eutectic point. Hence, nucleation and growth of IMCs were primarily governed by diffusion between Al and Mg atoms. In the present context, the ultrasonic addition in the FSLW process appears beneficial to reduce the IMCs in the weld zone. For example, a reduction in the IMC layer thickness with ultrasonic addition can be seen across the Al-Mg lapped interface (welds W#5 and W#6 in Figures 6(d) and 7(d)). Additionally, the SZ of W#4 shows minor traces of Al_3Mg_2 , which is consistent with the XRD results shown in Figure 14.

As reported by Lv *et al.*,^[28] the optimum value of heat input is advantageous to reduce the amount of IMCs during ultrasonic assistance. The acoustic addition serves two purposes. First, it improves the material flow,^[43,48] which does not permit stagnation of the constitutionally liquated material. Hence, the IMCs are shattered throughout the SZ.^[28,49] Second, it does not favor the eutectic transformation of the liquated material,^[28] which hinders the formation of IMC phases during its rapid cooling. Hence, depending on the process parameters, the weld strength of the U-FSLW joints is comparatively higher than that of the conventional joints. This observation is also consistent with the previous findings of Kumar *et al.* and Lv *et al.*^[28,29]

Table II. FSLW Tool Specifications^[29]

Tool Material	Shoulder Diameter (mm)	Shoulder Profile	Pin Profile	Major Diameter (mm)	Minor Diameter (mm)	Pin Length (mm)	Tool Hardness
H13 tool steel	20	concave	threaded tapered	5.8	3	5.6	62 HRC

Table III. Weld Specifications and Parameters Used (Welding Speed Is Constant = 100 mm/min)

Weld	Mode	Rotation Speed (rpm)	Tool Tilt Angle	Plunge Depth (mm)
W#1	no ultrasonic	600	3 deg	0.1
W#2	with ultrasonic	600		
W#3	no ultrasonic	800		
W#4	with ultrasonic	800		
W#5	no ultrasonic	1000		
W#6	with ultrasonic	1000		

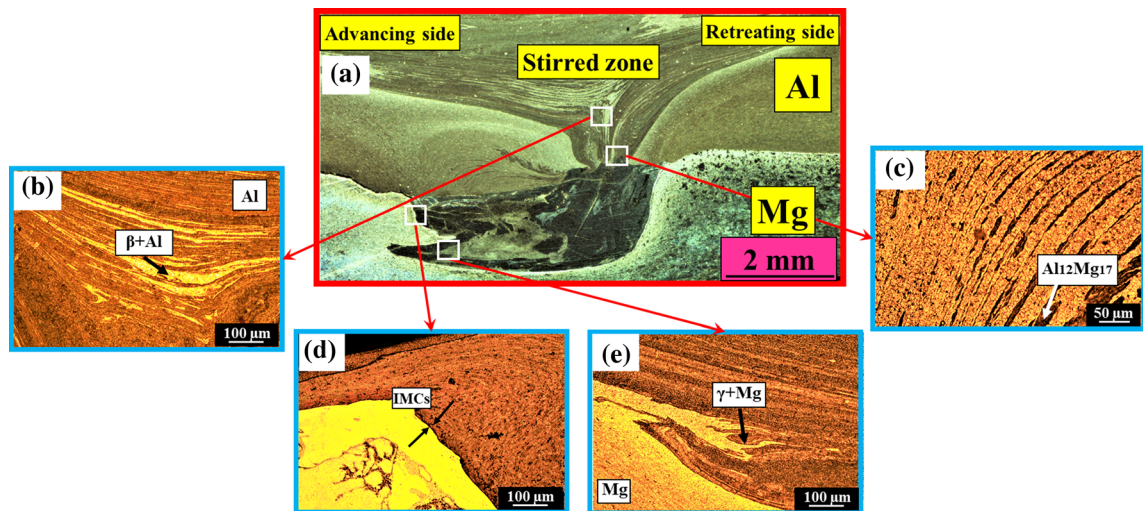


Fig. 2—Microstructure of transverse cross section of W#1 at (a) different regions and (b) through (e) correspondingly shown in higher magnification.

An intermixed complex vortex material flow pattern across the IMC region in the SZ is observed containing lamellar-shaped shear bands of Mg and Al (Figures 3(e), 5(f), 5(h), and 7(c)). The Al and Mg substrates are intermixed, stirred, and moved from left to right, top to bottom, and vice versa (Figures 4(d), (g), (i) and 5(d), (h), (i)), implicating an intricate material flow configuration. Massive intermetallic formation in conventional welds (W#3) and its subsequent fragmentation during the ultrasonic addition (W#4) can be seen in Figures 4 and 5.

The SZ microstructure of W#5 (Figures 6(a) and (c)) indicates the massive presence of thickened IMCs, primarily due to excessive heat input at higher rotation speeds. For welds W#3 and W#4, the material behavior adjacent to the SZ evidences dual flow characteristics (Figures 4(a), (d) and 5(a), (d), (g)). The first one is just beneath the shoulder surface, owing to frictional contact

between the shoulder and adjacent material. The second one arises adjacent to the pin surface and is stimulated by the twin effects of the torsional velocity field, followed by driving the material to push up and down owing to the pin thread action^[50,51] (depicted by red arrows and the dashed ellipse in the SZ in Figure 5(a)). The SZ of welds W#1 through W#6 (Figures 4(d) and 6(e)) shows a vortex flow pattern, known as the swirl zone, observed at the pin bottom. A similar phenomenon was also reported by Gerlich *et al.*^[50]

The ultrasonic vibrations can intensify the material pulsation^[24,25,52,53] and amplify the material flow across the SZ periphery (W#4 in Figures 5(f) and (g)). It is also attributed to the bulk material movement due to ultrasonically induced turbulence.^[25,54] The microstructure at the advancing side (AS) shows significant intermixing compared to that at the retreating side (RS)^[12,16,55] (Figures 2 to 7). The material flow pattern

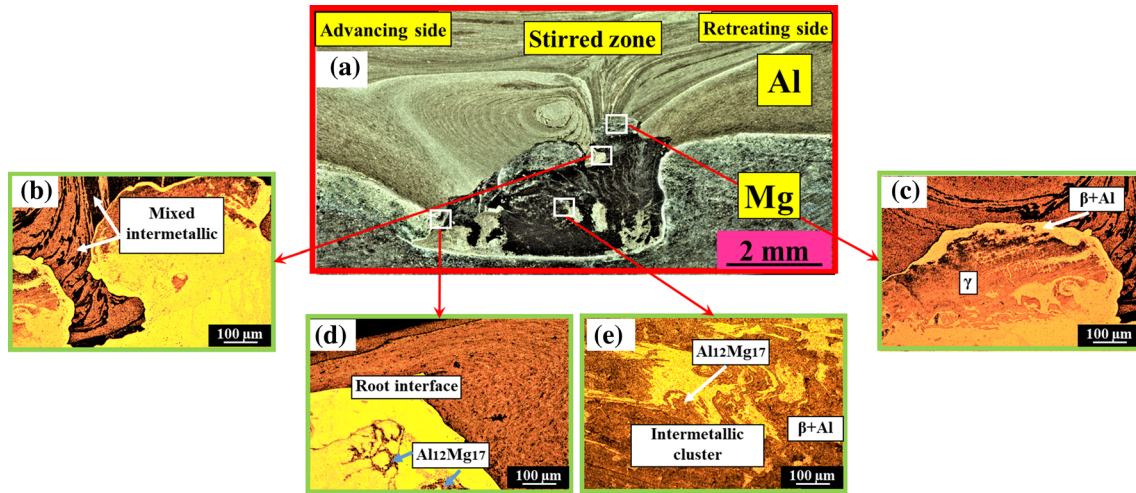


Fig. 3—Microstructure of transverse cross section of W#2 at (a) different regions and (b) through (e) correspondingly shown in higher magnification.

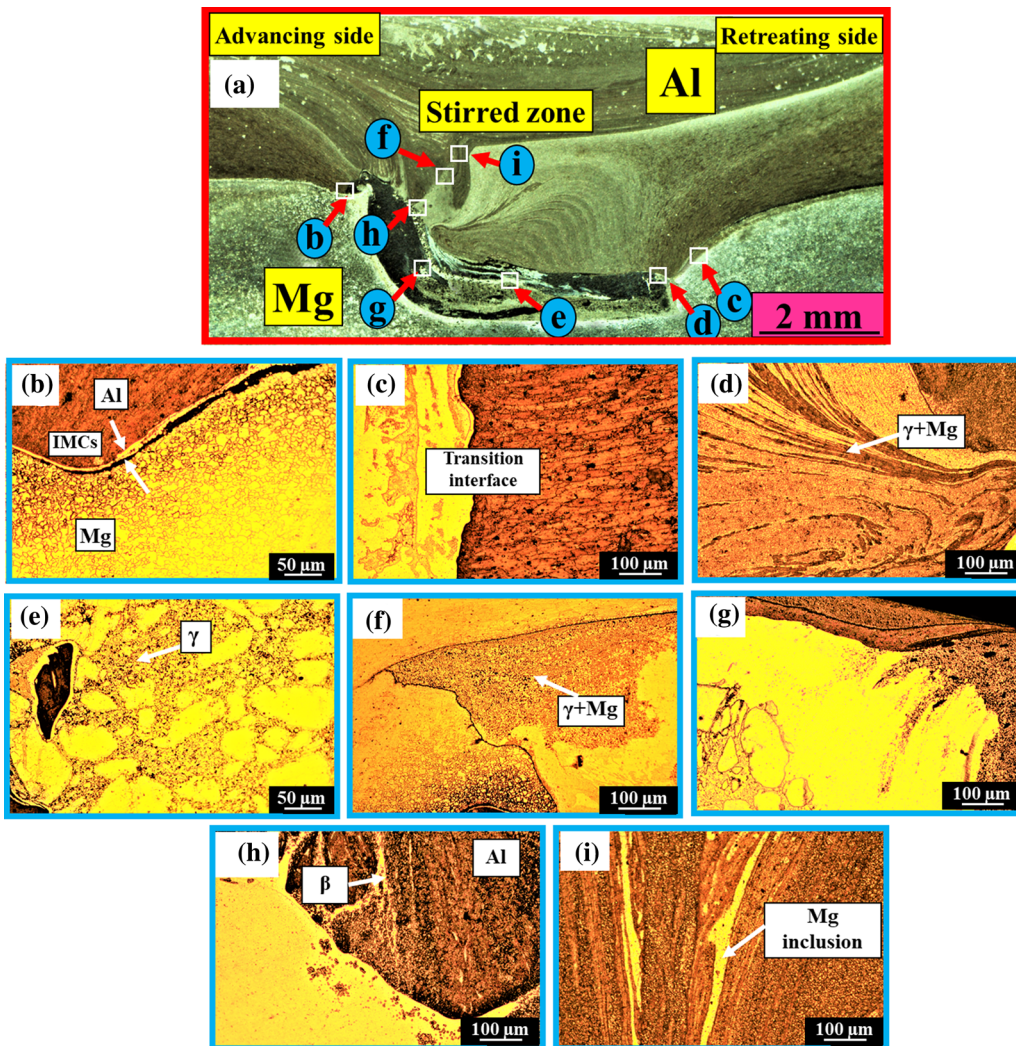


Fig. 4—Microstructure of transverse cross section of W#3 at (a) different regions and (b) through (i) correspondingly shown in higher magnification.

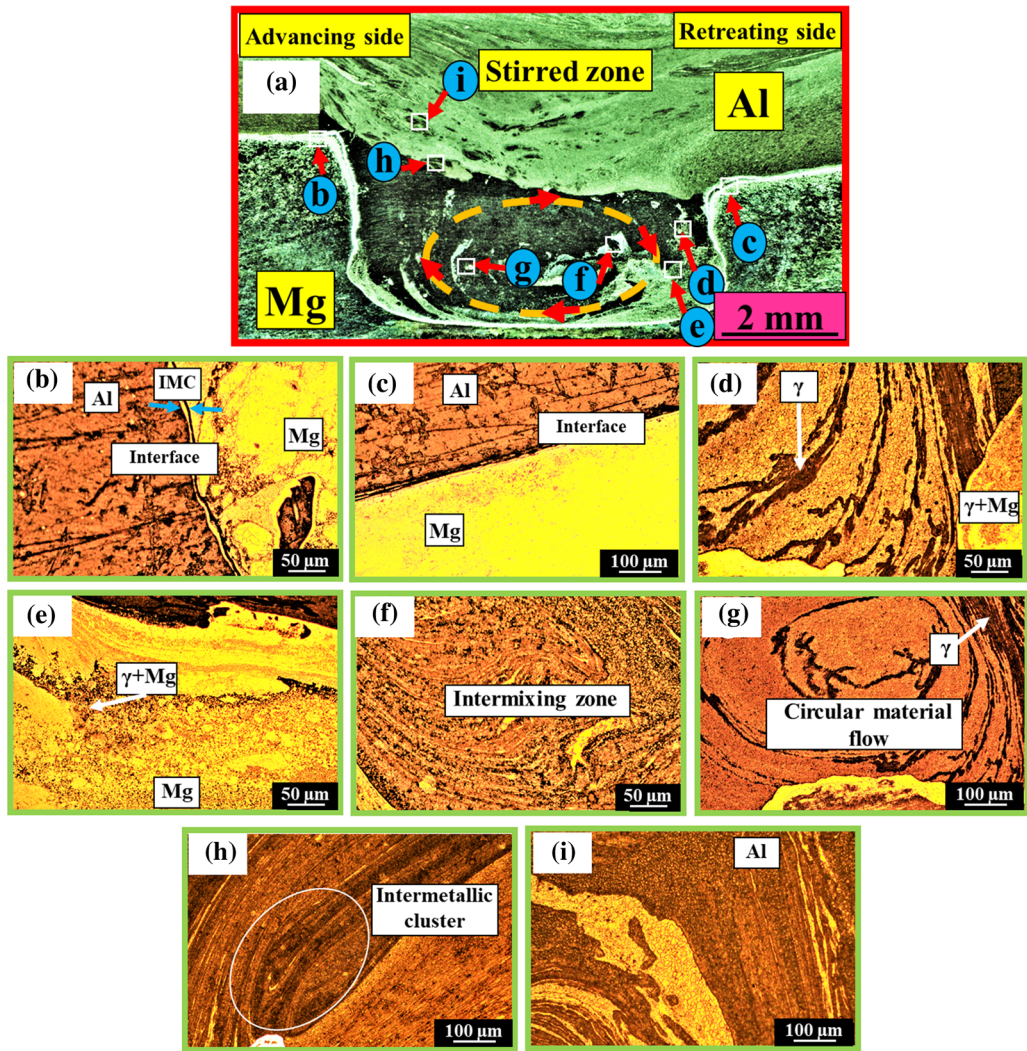


Fig. 5—Microstructure of transverse cross section of W#4 at (a) different regions and (b) through (i) correspondingly shown in higher magnification.

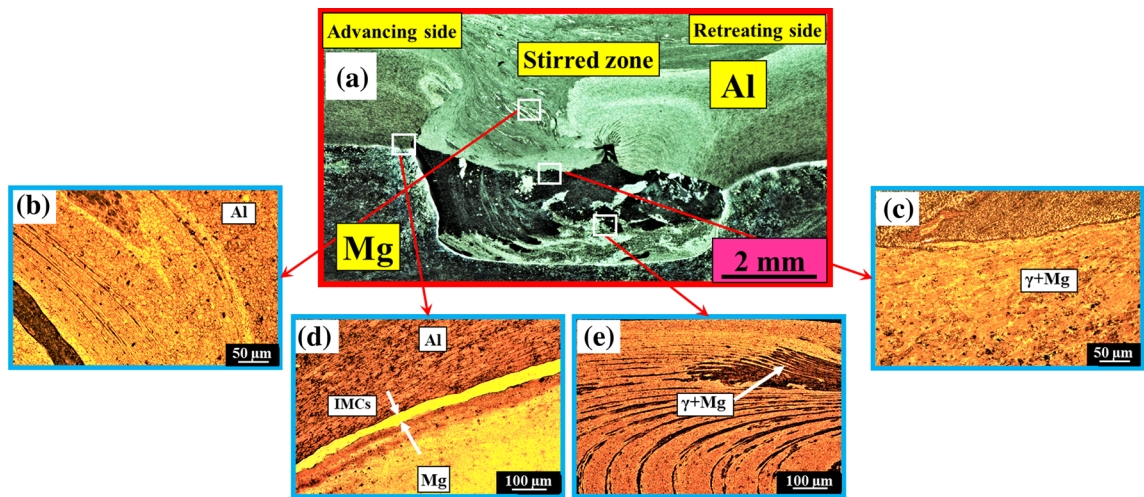


Fig. 6—Microstructure of transverse cross section of W#5 at (a) different regions and (b) through (e) correspondingly shown in higher magnification.

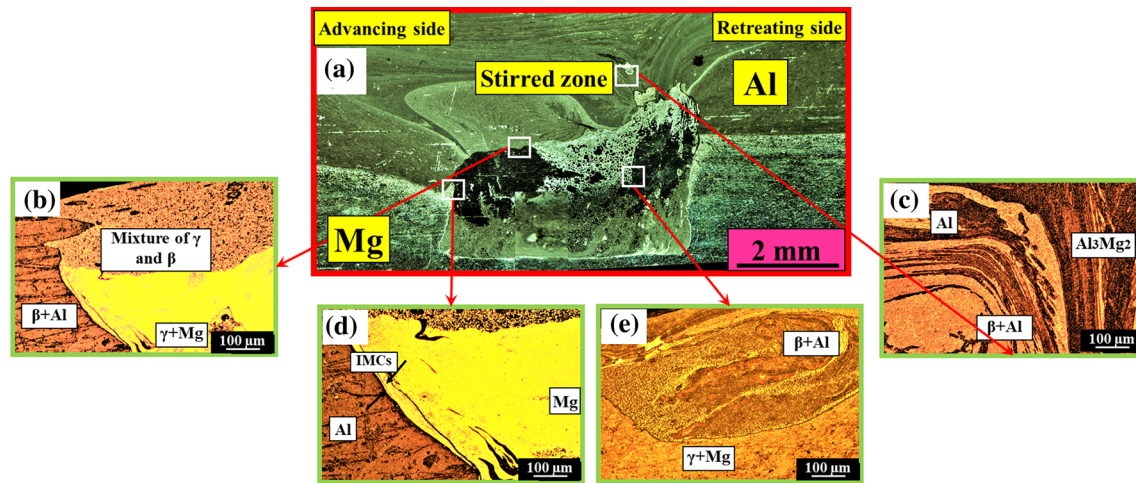


Fig. 7—Microstructure of transverse cross section of W#6 at (a) different regions and (b) through (e) correspondingly shown in higher magnification.

from the RS to AS resembles elongated bands of Al and Mg substrates, which are displaced toward the Mg region (Figures 2 to 7).^[56] Apparently, two regions of material flow are observed. First, just below the tool shoulder region, which pushed the material toward the AS. Second, at the pin bottom region, displacing the material upward^[57] (Figures 6 and 7).

As emphasized, acoustic energy is also productive in refining the grains. Irregular intermixing of both the metals is evident from Figures 3, 5, and 7, representing the formation of lamellae of distinguished phases. Chaotic intermixing and formation of alike intercalated structures are observed during dissimilar Al-Mg welding.^[58] The ultrasonic addition has facilitated equiaxed and enriched intermixing of both alloys and exhibits the formation of finely shaped lamellae (Figures 5(b) and (f)).^[50,51] Thick flocks of IMCs are also apparent in the SZ, primarily adjacent to the Al surface and the region of the dark-itching layer observed in the Mg-rich zone (Figures 4(f), (i) and 6(c)). With the addition of ultrasonic vibrations, the branches of IMC clusters are fragmented and dispersed unequally within the SZ (Figures 5(d), (g), and (f)).^[28,59] It should be noted that Al and Mg alloys have variable responses with respect to etchants into weldment, thereby showing different dark regions in the lower magnification images for FSLW and U-FSLW joints.

B. Scanning Electron Microscopy Studies

The SEM images and intermetallic phase analysis of the transverse cross section of W#3 and W#4 at different regions are marked in Figures 8(a) and 9(a) and correspondingly shown in higher magnification (Figures 8(b) through (k) and Figures 9(b) through (k)). To identify the weight percentage composition of chief constituents and dissociate various phases formed, the EDS point scan of the selected region is also carried out (Tables IV and V). The SZ contains a mixture of Al, Mg substrates, and complex lamellae that could settle at the bottom during the FSLW process (Figures 8(e), (f)

and 9(f), (g)). The SEM trajectory of joints W#3 and W#4 shows a comparatively broad plateau and SZ boundary of acoustic welds (Figures 8(a) and 9(a)). The ultrasonic vibrations add material pulsation, consenting to its forced and speedy transportation from one region to another in the SZ (Figures 9(c) and (e) through (k)). Under the vibratory action of the welding tool, some material is pulled out from the lapped regions, intermixed, and settled at the bottom (Figures 9(d), (e), (f), and (g)), thus reinforcing the weldment strength.^[29]

For weld W#3, the material flow pattern is comparatively linear (Figures 8(f), (g), (i) and 10(b)), which restrains the intermixing and transportation of the Al and Mg substrates from one region to another. Therefore, similar substrate clotting (Figures 8(c) and (d)) makes the dissimilar interface weak and reduces the joint strength significantly. The SZ for both the welds (W#3 and W#4) shows grains of Mg alloy, $Al_{12}Mg_{17}$, and $Al_{12}Mg_{17} + Mg$ eutectic with a minor percentage of Al_3Mg_2 (Figures 8(b) to (k) and 9(b) to (k)). It is also confirmed by EDS analysis of regions of interest marked by points 1 through 7 in Figures 8 and 9. The formation and, after that, the nucleation of IMC phases in the lapped region can be understood by the fact that when SZ temperature crosses the eutectic temperatures, atoms of both alloys attempt to diffuse into each other and favor the IMC formation during cooling.^[16] It has been mentioned that the nucleation and subsequent growth of IMC layers can substantially degrade the Al-Mg alloy weldment strength.^[14,16,60]

The nature of IMCs formed pointedly depends on the weight percent of different alloys and their corresponding compositions,^[16] as evident in Tables IV and V. The acoustic assistance improves the hook features, restrains the eutectic transformation of the liquated material,^[28] and shatters the IMC branches, which all together hinder the IMC formation and stagnation, thus improving the weld quality.^[28,29] The absence of eutectic transformation may be due to rapid cooling of the liquid L from a very high temperature, which continues to be quick at both the eutectic temperatures. During

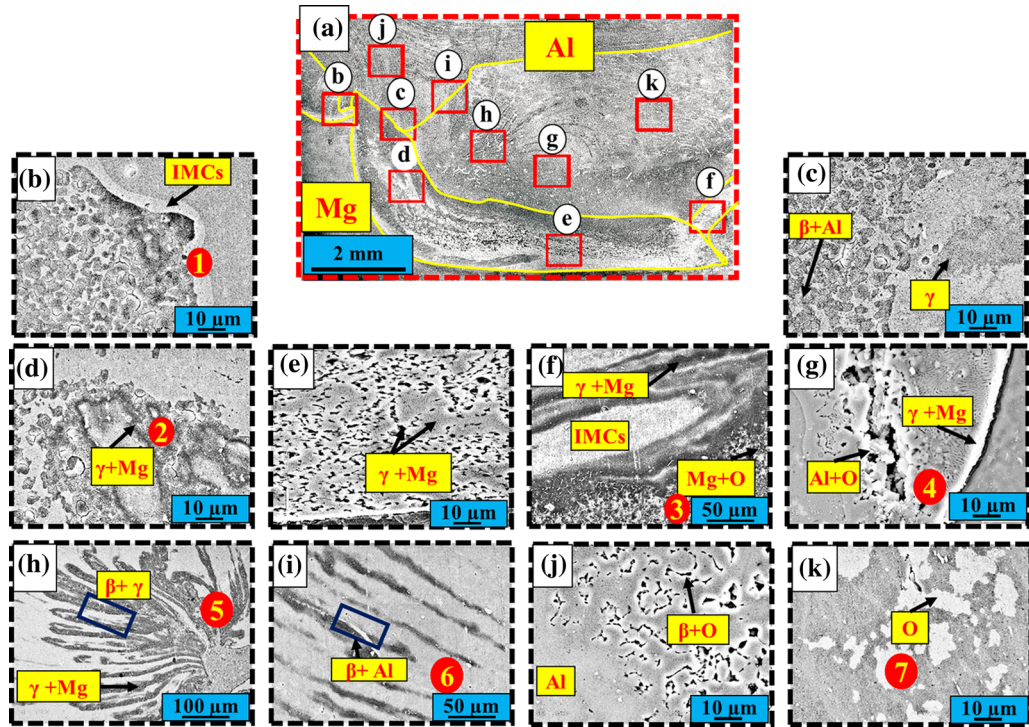


Fig. 8—SEM imaging and intermetallic phase analysis of transverse cross section of W#3 at (a) different regions and (b) through (k) correspondingly shown in higher magnification.

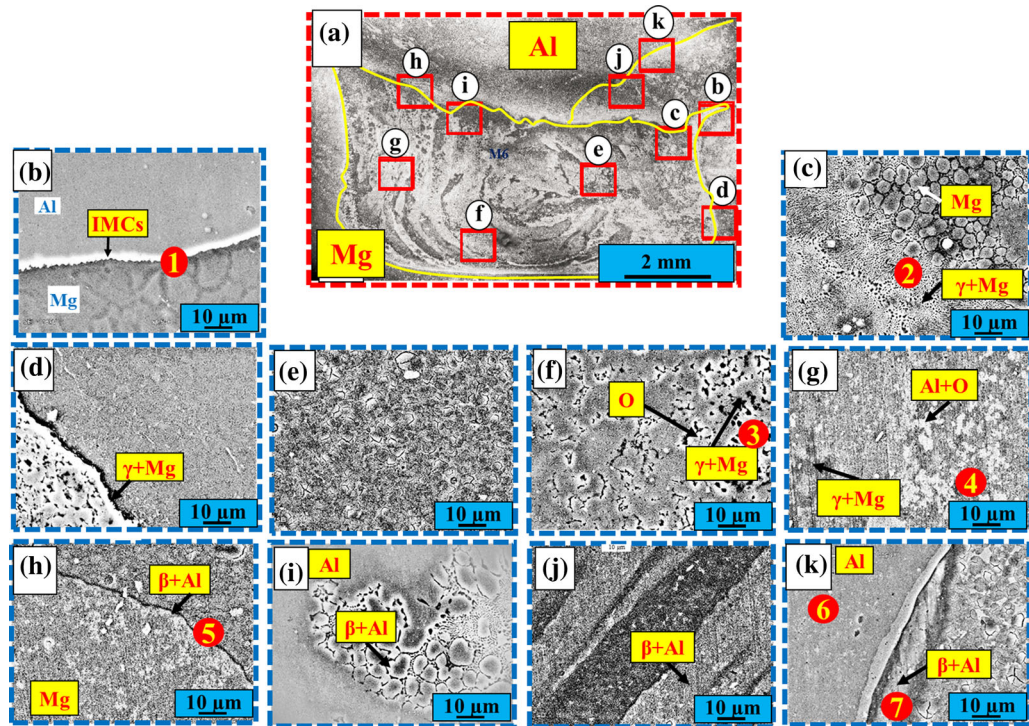


Fig. 9—SEM imaging and intermetallic phase analysis of transverse cross section of W#4 at (a) different regions and (b) through (k) correspondingly shown in higher magnification.

ultrasonic addition, it appears that the subsequent rapid cooling of the liquid L does not favor the eutectic transformations, $L \rightarrow Al_3Mg_2 + \alpha-Al$ at $450^\circ C$ and $L \rightarrow Al_{12}Mg_{17} + \alpha-Mg$ at $437^\circ C$.^[28]

Figures 10(b) and (c) show the material flow characteristic and intermixing behavior of dissimilar Mg and Al alloys for the selected regions, marked in Figure 10(a) (with yellow-colored circles). Subsequent

Table IV. Weight Percentage Composition of Different Points Marked in Fig. 8

Point	Mg	Al	Si	Fe	Cu	Zn	Mn	O	Total	Phase
1	35.21	56.12	0.2	0.19	0.19	0.55	0.39	5.65	98.5	Al ₃ Mg ₂
2	57.12	35.15	0.03	0.02	0.04	0.69	0.51	6.18	99.74	Al ₁₂ Mg ₁₇
3	86.55	11.43	0.02	0.025	0.01	0.43	0.12	1.59	100.175	AZ31B Mg
4	36.11	52.12	0.33	0.21	0.22	0.54	0.51	11.56	101.6	Al ₃ Mg ₂
5	32.12	59.12	0.25	0.11	0.23	0.48	0.61	7.02	99.94	Al ₃ Mg ₂ + Al
6	11.14	83.41	0.021	0.11	0.02	0.62	0.49	4.04	99.851	AA6061-T6
7	15.24	24.19	0.15	0.22	0.01	0.41	0.58	59.25	100.05	oxides

Table V. Weight Percentage Composition of Different Points Marked in Fig. 9

Point	Mg	Al	Si	Fe	Cu	Zn	Mn	O	Total	Phase
1	43.31	50.11	0.2	0.19	0.19	0.55	0.39	5.65	100.59	Al ₃ Mg ₂
2	59.14	32.15	0.15	0.15	0.03	0.72	0.47	6.81	99.62	Al ₁₂ Mg ₁₇
3	65.87	30.44	0.07	0.02	0.19	1.02	0.09	1.45	99.15	Al ₁₂ Mg ₁₇ + Mg
4	56.89	36.15	0.03	0.09	0.01	0.9	0.1	4.85	99.02	primary Al ₁₂ Mg ₁₇
5	38.19	57.32	0.31	0.11	0.11	0.47	0.09	3.54	100.14	primary Al ₃ Mg ₂
6	16.07	80.51	0.07	0.16	0.18	0.87	0.5	1.19	99.55	AA6061-T6
7	34.4	57.41	0.77	0.51	0.15	0.2	0.18	6.15	99.77	Al ₃ Mg ₂ + O

intermixing of both Al and Mg substrates is evident. However, the particle distribution of Mg in the Al substrate region is comparatively higher than that of Al particles in the Mg substrate region. It shows that during the FSLW process, a mixed microstructure of dissimilar alloys is formed adjacent to the bonded interface region. This finding backs the theory that the welding tool can induce a plastic flow pattern across the adjoining metals because of mechanical stirring.

With ultrasonic assistance, the blending intensity of Al and Mg is increased (red and blue regions (Figure 10(c))), while the material flow pattern forms vortex loops. This could be due to the material pulsation and thermo-mechanical-acoustic effects induced in the SZ.^[26] The acoustic addition can be thought of as beneficial as it can reduce the flow stresses, improving the material flow and suppressing the weld defects.^[28,36,38,43]

The EBSD image analysis (location is marked in Figure 10(a) with the blue colored rectangle) is also conducted across the Al-Mg alloy interface to detect any probable texture and IMCs that might have influenced the ultrasonic assistance (Figures 11 and 12). The interfacial microstructure of the ultrasonic joint is shown in Figure 11, in which the blue and red colors correspond to the Al and Mg substrates while the yellow denotes the Al₁₂Mg₁₇ IMC phase. The interface shows the shattering of the Al₁₂Mg₁₇ IMC phase, possibly due to intensive ultrasonic action. This observation further backs our previous findings that ultrasonic addition can shatter and fragment the IMC phases across the weld interface.^[40]

Figure 12 shows the (100) (110) (111) pole figures of the Al₁₂Mg₁₇ IMC phase, Al, and Mg substrates derived from the EBSD map of the SZ interface, as shown in

Figure 11. Despite the columnar grain orientation, the pole figures show an arbitrary spread of Al, Mg substrate textures. The oriental distribution of the Al₁₂Mg₁₇ phase is also unsystematic, with the meek affinity of {100} and {111} fiber texture revealed. The axis is vertical to the dissimilar interface plane, *i.e.*, the RD-TD plane of the BMs. It is interesting to note that no such appearance is visible for the Al₃Mg₂ IMC phase along the interfacial plane, signifying a complete elimination of the β phase. The major affinity of Mg columnar grain with respect to the Al illustrates its higher flow rate and accumulation along the interface region.

In a nutshell, the outcomes signify that the acoustic addition not only fragments or suppresses the IMC phase but can also wipe it out completely. The pole figures point out that the Al₁₂Mg₁₇ phase grows approximately as a random texture, while the formation of a columnar structure may be due to Al-Mg diffusions.

C. Weld Strength and Fractography

To formulate a correlation of weld microstructure, IMCs, and weld strength, it becomes vital to add a discussion on the weldment mechanical properties. Figure 13 shows a comparison plot of the weld shear strength of friction-stir-lap-welded joints based on the present and previously reported work.^[61] The detailed analysis of the weld shear strength for different process parameters has already been documented elsewhere by the authors,^[29] hence, it is omitted here. In the authors' findings, the maximum shear load during ultrasonic assistance (W#4) is ~2.45 kN, which is marginally higher than reported by Ji *et al.*^[61] Without ultrasonic addition, the Al/Mg lap joint can have a shear strength of ~1.95

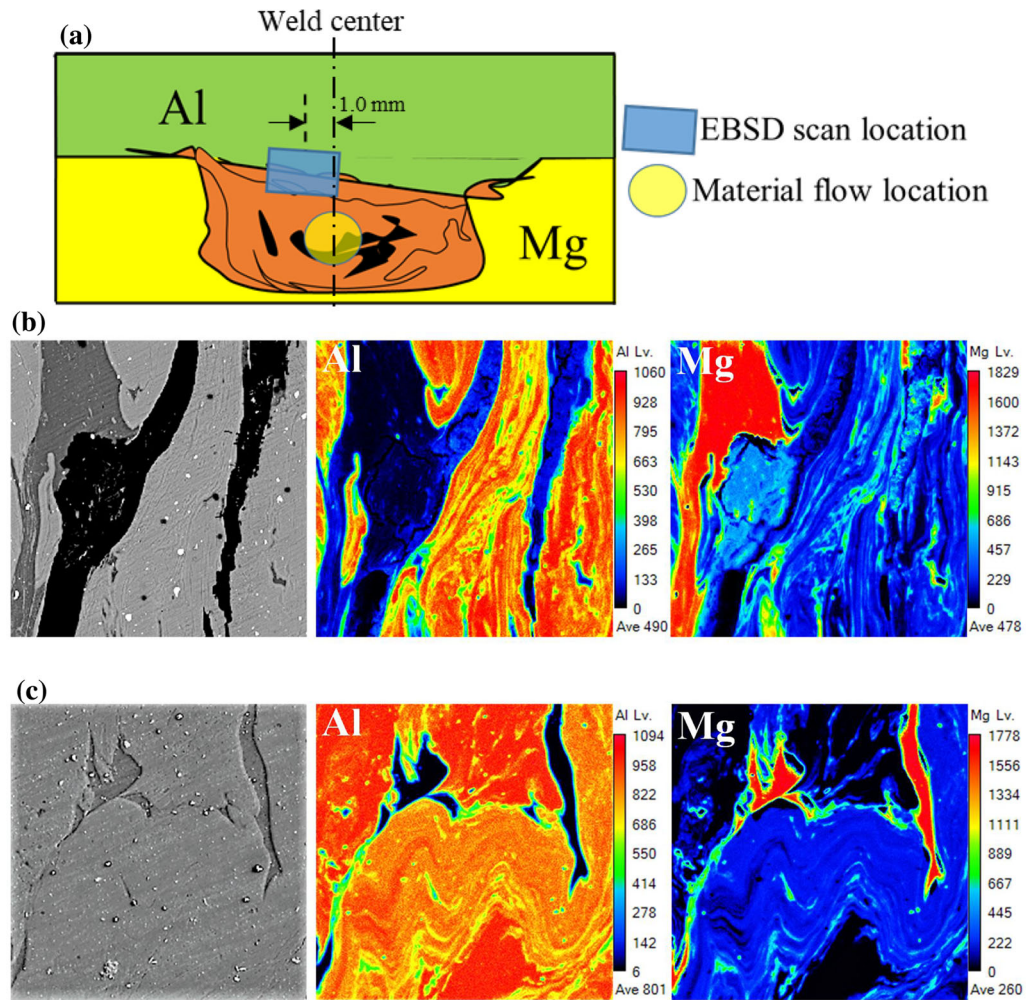


Fig. 10—(a) EBSD and material flow locations and material mapping of (b) W#3 and (c) W#4.

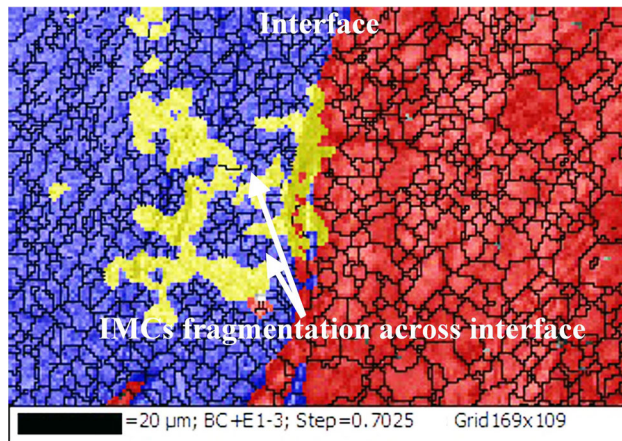


Fig. 11—High-resolution EBSD map of the ultrasonic weld interface.

kN, which is significantly lower than its counterpart. This signifies that acoustic assistance can enhance the weld strength because of better material flow, reduction in weld anomalies (as discussed in Section B),^[62] and suppression of IMC phases.^[28] This fact is also consistent with the previous finding reported elsewhere.^[25]

In order to further verify the remark of IMC reduction due to ultrasonic addition, the XRD pattern analysis of weld joints W#3 and W#4 is made, and the outcomes are presented in Figure 14. The SZ shows the adequate intermixing of both Al and Mg substrates. Comparatively, higher peaks of dual IMC phases $\text{Al}_{12}\text{Mg}_{17}$ and Al_3Mg_2 are observed for the conventional joint (W#3). The dual IMC phases also characterize the ultrasonic joint. However, their peak intensities are significantly shorter. The Al_3Mg_2 IMC phase is hardly found in the XRD scan for the ultrasonic joint, while the $\text{Al}_{12}\text{Mg}_{17}$ phase is found to be randomly distributed. This signifies that the acoustic assistance not only suppresses the IMC intensities but also modifies the reaction rate to cause Al_3Mg_2 phases to vanish.

The XRD spectrum also predicts the nonuniform distribution of IMCs across the SZ and consists of a major proportion of the $\text{Al}_{12}\text{Mg}_{17}$ phase.^[12,16] The process of IMC reduction can be attributable to the controlled interdiffusion of both the metals across their interfaces (as observed in Section A) and their shattering under the ultrasonic influence. Among the two IMC phases ($\text{Al}_{12}\text{Mg}_{17}$ and Al_3Mg_2), the Al_3Mg_2 has been reported to be extraordinarily brittle and primarily

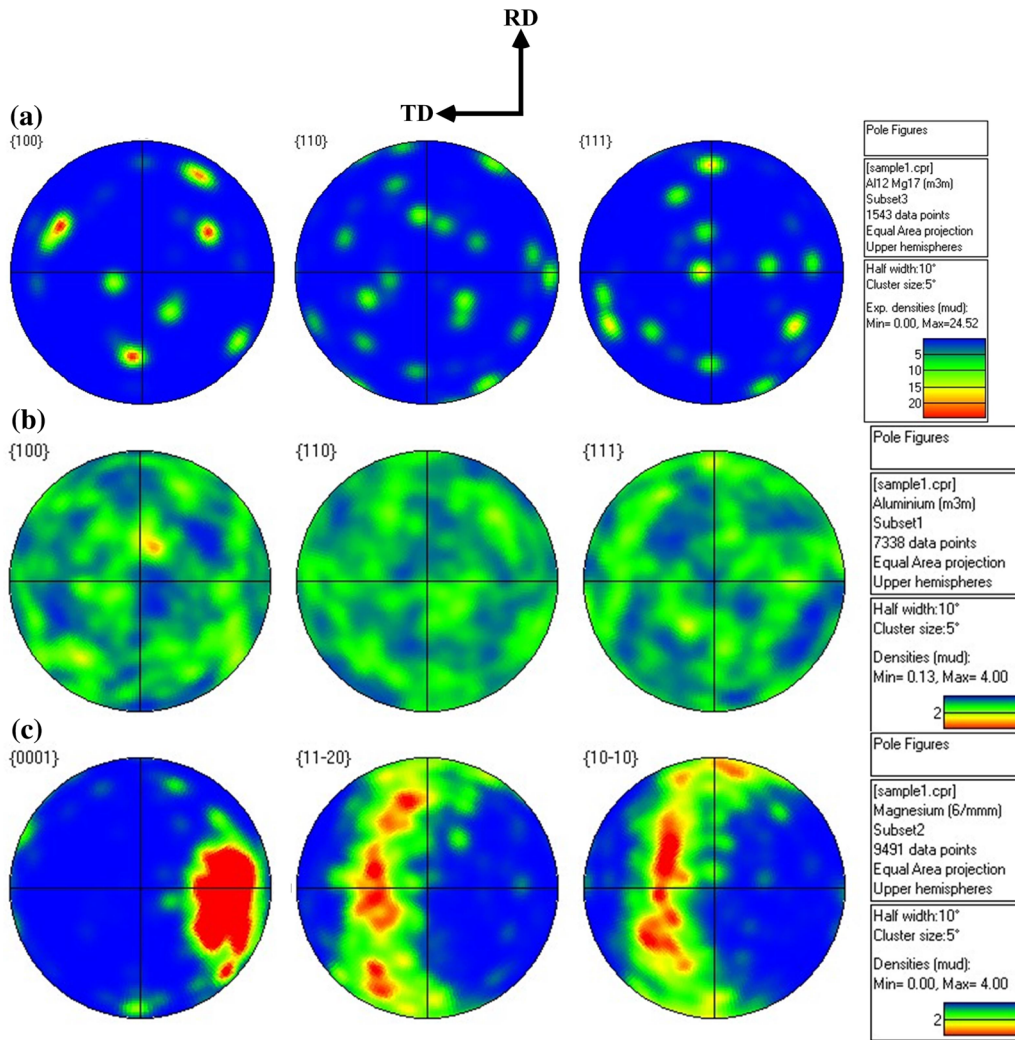


Fig. 12—Pole figures of (a) $Al_{12}Mg_{17}$, (b) Al, and (c) Mg across the interface, as shown in Fig. 11.

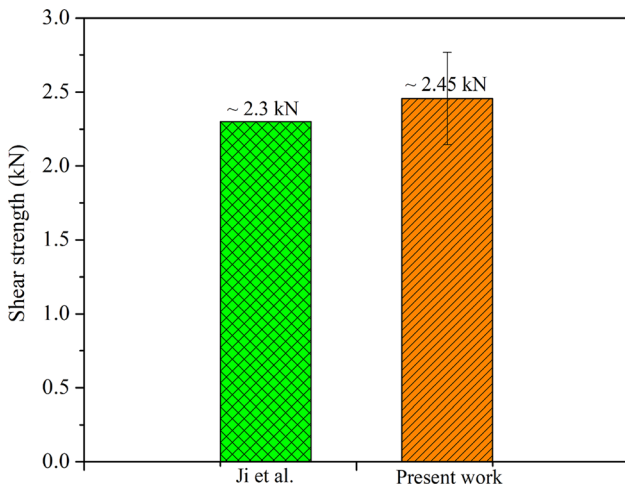


Fig. 13—Weld shear strength comparison.

responsible for deteriorating weld strength.^[16] The depletion of the Al_3Mg_2 phase during acoustic assistance can be thought of as beneficial for better weld

quality; hence, the weld strength of ultrasonic joints is reported to be higher.

The influence of ultrasonic vibrations on the IMC formation can also be quantified by microhardness analysis of the weld section, as shown in Figure 15. As observed, in both cases (FSLW and U-FSLW), the weld central regions have the maximum microhardness. The reason for this is attributed to the heavy accumulation of brittle IMC phases (Al_3Mg_3 and $Al_{12}Mg_{17}$) under extensive blending of Al and Mg substrates in the SZ. As reported previously,^[63] the Al_3Mg_3 phase has hardness several folds higher than $Al_{12}Mg_{17}$ and the base metals (BMs). That is why the SZ of both joints has higher hardness compared to the BMs.

It is interesting to note that the Al side SZ has higher hardness than the Mg region. This is because the Al-rich regions favor Al_3Mg_2 formation. Contrary to that, the Mg-rich SZ encounters lower hardness due to the possible presence of $Al_{12}Mg_{17}$ phase. The SZ microhardness of ultrasonic joints replicates a marginal reduction in the hardness region (red region in Figure 15(b)), possibly due to the reduced presence of

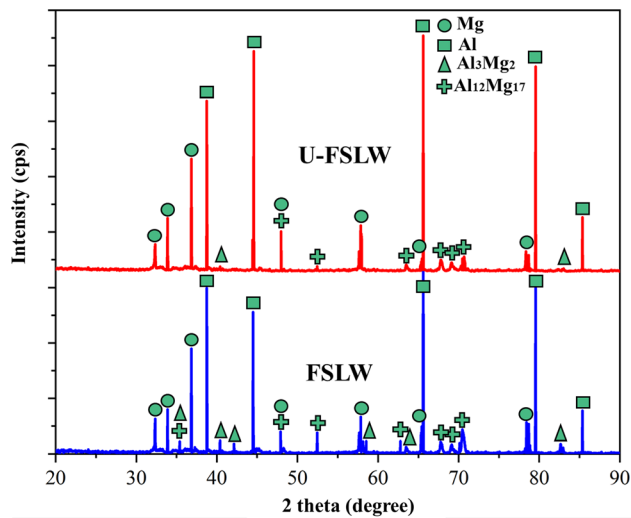


Fig. 14—XRD results of the SZ for W#3 and W#4.

Al_3Mg_2 . Thus, the ultrasonic action favors $\text{Al}_{12}\text{Mg}_{17}$ formation while suppressing the Al_3Mg_2 phase. The joints treated with acoustic assistance have a maximum microhardness of 189.5 HV, which is 16.5 HV lower than that of their counterparts.

To analyze the fracture behavior of the weld joints under different parameters, a detailed investigation of welds W#1 through W#4 was drafted in this section. Various regions of interest are marked in the micrographs (shown as hollow rectangles) and, subsequently, shown in higher magnification (Figures 16(a), (b) and 17(a), (b)). As evident, most of the FSLW joints failed *via* brittle fracture. Their failure mode portrays the dual-path crack propagation through lap interface and prominent fracture observed across the dissimilar metal interface (Figures 16(a) and 17(a)). The inadequate and insufficient intermixing of both the metals results in weak bond formation, which results in the brittle failure.^[51] To gain further insight into fracture properties, various regions are marked (with hollow rectangles and labeled 1 through 8) in micrographs and correspondingly shown in Figures 16(a), (b) and 17(a), (b).

Irrespective of the welding parameters used, most of the samples in SEM scans show the river flow pattern associated with the cleave formation and fissures across the weldment regions^[64] (SEM images (1) and (3) shown in Figure 16(a) and SEM images (2) and (4) shown in Figure 17(a)). The presence of fluffy voids and tearing ridges (SEM image (2) shown in Figure 16(a) and SEM image (1) shown in Figure 17(a)) can also be thought of responsible for degrading the weldment load-carrying capacity. The crack is observed to be initiated across the regions having an enormous amount of IMCs in the SZ (Figures 16(a) and 17(a)). This statement is also consistent with the previously published reports.^[14,15] The hardness of IMCs (Al_3Mg_2) is several times higher than that of BMs, which hinders its elongation during shear testing^[14] and points toward the primary cause of crack initiation in high IMC regions. Moreover, the tendency of retaining a higher stress concentration of the Al_3Mg_2

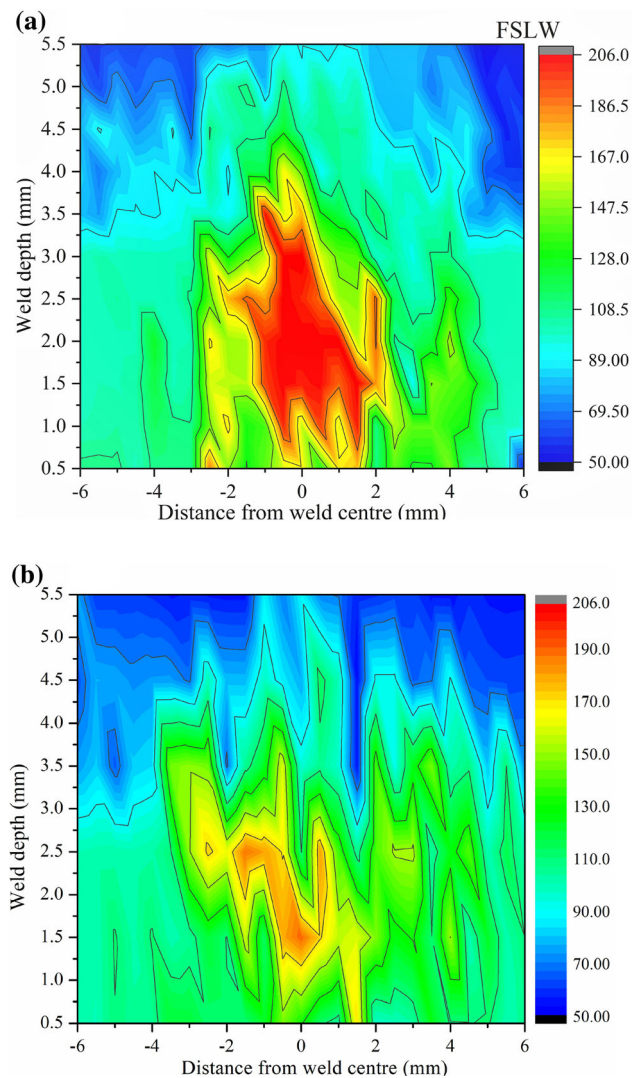


Fig. 15—Microhardness profile for (a) W#3 and (b) W#4.

IMC phase attracts lateral cracking,^[16] hence making a weak section of the lapped joint.

Due to IMC phase brittleness, the joints are susceptible to fail without any appreciable elongation during shear testing. In short, it can be emphasized that FSLW samples undergo brittle fracture, which is a primary characteristic of the IMC presence and provides an easy path for crack propagation across Al and Mg alloy fracture interfaces. The magnitude of lap shear fracture load depicts the intensity of localized material deformation across the heat-affected zone and thermomechanical-affected zone (TMAZ),^[65] which have the weakest regions in the weld and render an easy path for crack formation and its propagation.^[65,66] It is interesting to note that several joints exhibit some amount of necking during ultrasonic assistance and undergo mixed fracture mode, *i.e.*, brittle and ductile fracture (Figures 16(b) and 17(b)). Besides, the SEM analysis of their fractured regions shows fine and swallowed dimples across the detached regions (SEM images shown by regions (5) through (8) in Figures 16(b) and 17(b)).

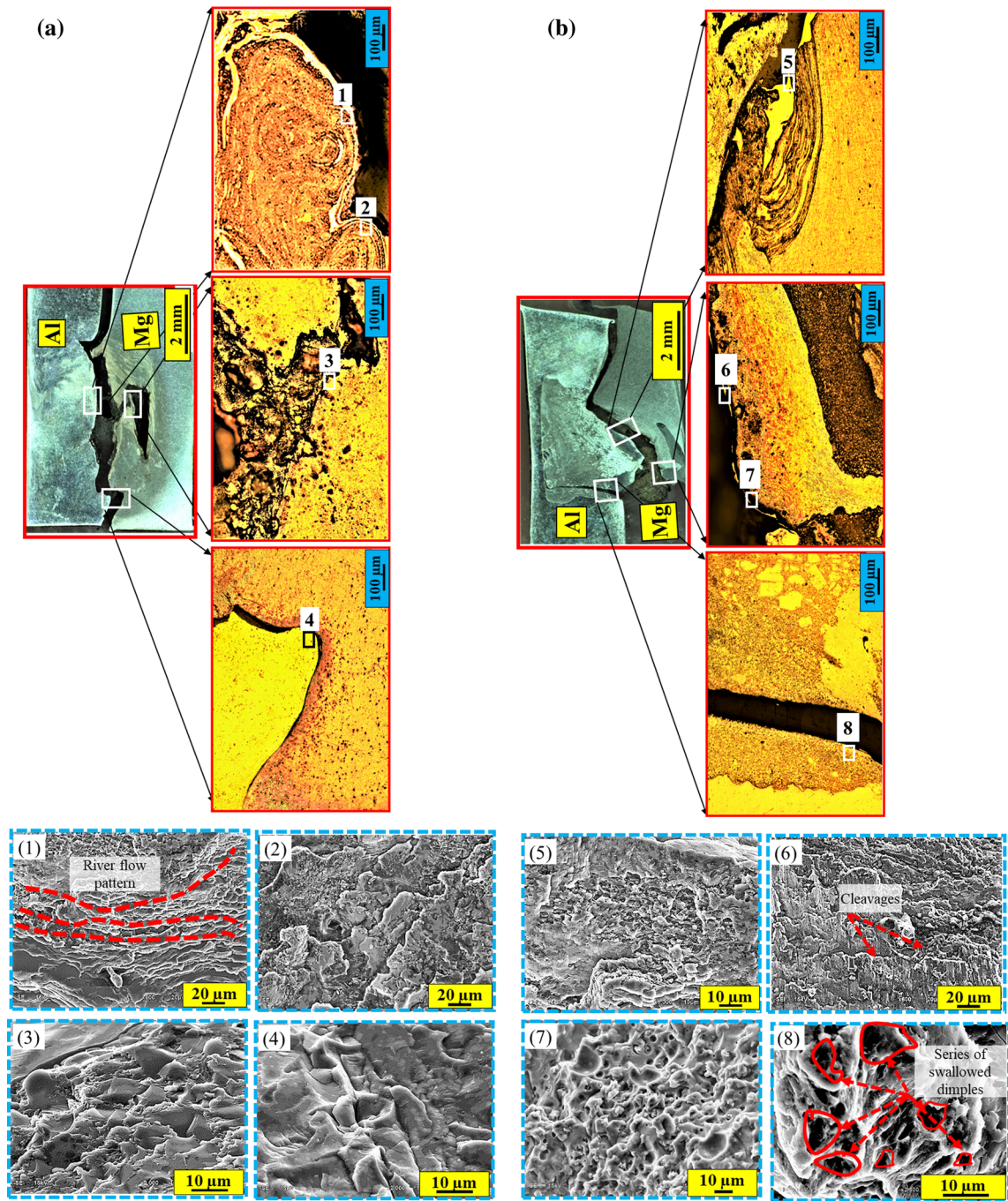


Fig. 16—Macrographs with regions of interests (marked with colored hollow rectangles in macrographs) and corresponding images in higher magnification of fracture samples (a) W#1 and (b) W#2. The SEM images are magnified views of various regions (1 through 8) marked in W#1 and W#2 micrographs.

Apparently, a moderate concentration of deep dimples is formed in the fracture regions, replicating a distinctly ductile fracture mechanism^[27,67] (SEM image (8), as marked in Figures 16(b) and 17 (b)). The shear necking followed by swallowed dimples raises the possibility of intensive plastic deformation of the metal due to acoustic assistance.^[27] The phenomenon of enhanced plastic deformation and material mixing due to ultrasonic vibration was reported in past literature.^[29]

The EDS analysis of fracture regions of Al and Mg sides (not shown here) confirms the single or dual IMCs; however, their elemental composition varies from region to region, thus varying the nature of the failure mechanism.

At acoustic territories, the refinement of Mg grains, shattering of IMCs across the SZ and interfaces, hinders the continuous propagation of cracks and, hence, offers resistance to shear.^[28] The SEM scans of the ultrasonic

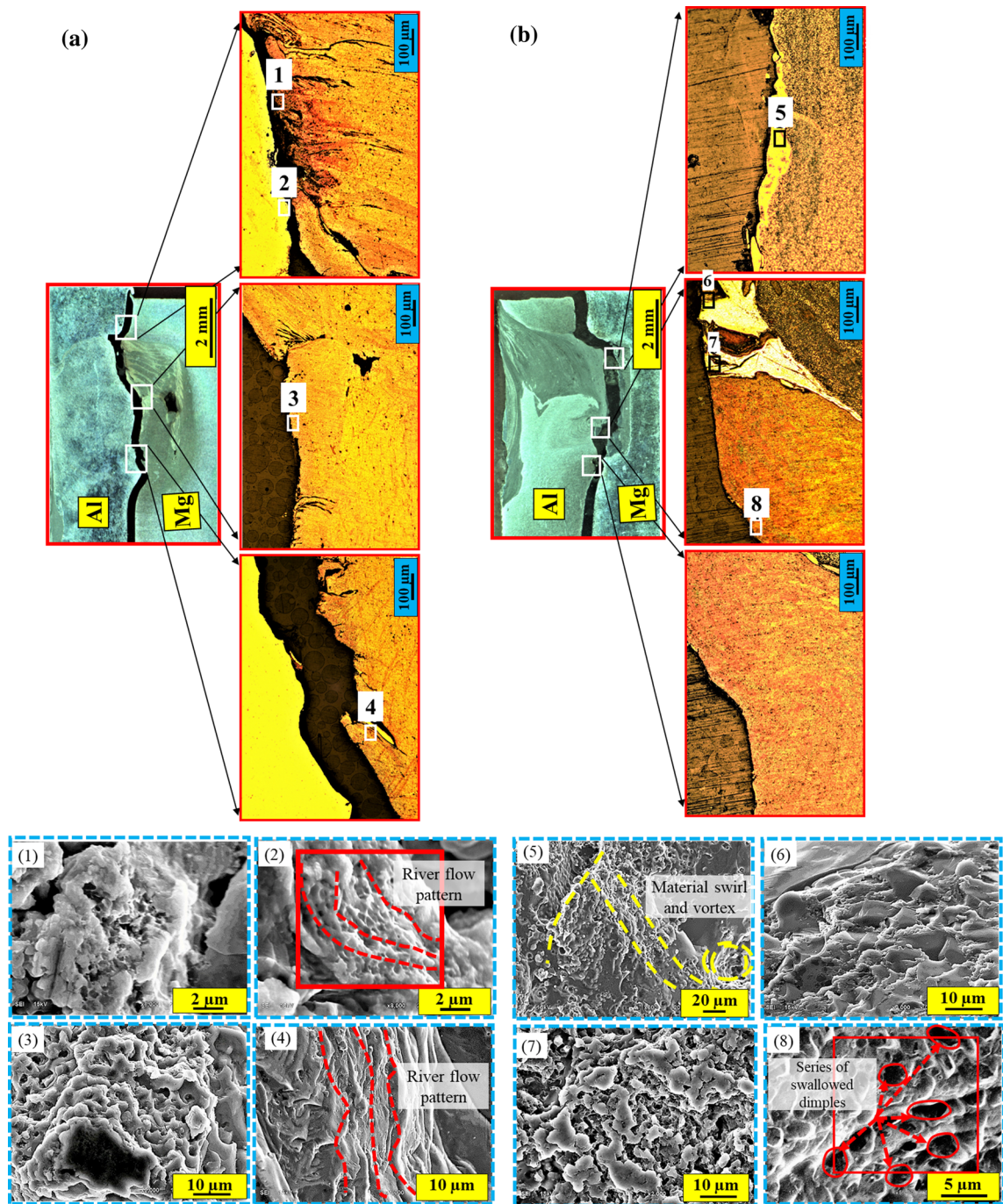


Fig. 17—Macrographs with regions of interest (marked with colored hollow rectangles in macrographs) and corresponding images in higher magnification of fracture samples (a) W#3 and (b) W#4. The SEM images are magnified views of various regions (1 through 8) marked in W#1 and W#2 micrographs (Color figure online).

joints reveal a dual mode of fracture with dimple fracture and cleavage (images shown by regions (5) through (8) in Figures 16(b) and 17(b)). This signifies that the regions where acoustic influence is maximum undergo intense material plasticization, vulnerable to dual fracture mode. As reported in the present work, the weld sample treated with acoustic assistance can have the highest average failure load, 2.45 kN. This reporting

emphasizes that a higher amount of shear load is required for the acoustic assisted sample with the highest failure energy and vice versa.

All of these outcomes confirm that acoustic assistance has a significant impact on weldment characteristics and improves the weldment ductility due to the higher fracture shear load and a ductile cleavage fracture mechanism.

IV. CONCLUSIONS

In this article, we have successfully obtained the dissimilar FSW of AA6061-T6 and AZ31B Mg alloys with and without the addition of ultrasonic vibrations. The main outcomes of the aforesaid investigation can be summarized as follows.

1. The acoustic assistance has effectively improved the material flow and intermixing across the SZs of the Mg and Al layered structures. Consequently, the homogeneous intercalated lamellae of dissimilar alloys are formed and distributed in the SZs of lapped regions.
2. The mechanical interlocking across the dissimilar lapped interfaces is improved, and weldment morphology became symmetric due to acoustic turbulence in the weld region. The SZ of the Al side has reported higher microhardness than that of the Mg side due to the formation of the brittle Al_3Mg_2 IMC phase at the Al-rich region. The maximum microhardness in the ultrasonic joint is lower than that of the conventional joint by 16.5 HV.
3. The SZs of both conventional and ultrasonic joints observed the presence of dual IMCs. However, XRD spectrum analysis confirmed a sharp reduction in peak heights and distribution of IMC phases across the SZ of ultrasonic joints compared to their counterparts.
4. The fracture samples are failed in the regions, having a higher accumulation of IMC phases. The acoustically treated fracture samples showed the swallow, deep dimples signifying the mixed mode of fracture pattern.

ACKNOWLEDGMENTS

The authors acknowledge the financial support from the National Natural Science Foundation of China (Grant No. 52035005) and the Key R&D Program of Shandong Province in China (Grant No. 2018GGX103001).

REFERENCES

1. S. Sree Sabari, S. Malarvizhi, and V. Balasubramanian: *J. Manuf. Process.*, 2016, vol. 22, pp. 278–89.
2. S. Kumar and C.S. Wu: *J. Harbin Inst. Technol.*, 2017, vol. 24, pp. 1–37.
3. A. Kar, S. Malopheyev, S. Mironov, R. Kaibyshev, S. Suwas, and S.V. Kailas: *Mater. Charact.*, 2020, vol. 171, art. no. 110791.
4. V.K. Yadav, V. Gaur, and I.V. Singh: *Mater. Sci. Eng. A*, 2020, vol. 779, art. no. 139116.
5. A. Kar, D. Yadav, S. Suwas, and S.V. Kailas: *Mater. Charact.*, 2020, vol. 164, art. no. 110371.
6. X.C. Liu, Y.F. Sun, T. Nagira, K. Ushioda, and H. Fujii: *Sci. Technol. Weld. Join.*, 2019, vol. 24, pp. 352–59.
7. J. Dong, D. Zhang, W. Zhang, W. Zhang, and C. Qiu: *J. Mater. Sci.*, 2019, vol. 54, pp. 11254–62.
8. A.P. Zykhova, S.Y. Tarasov, A.V. Chumaevskiy, and E.A. Kolubaev: *Metals (Basel)*, 2020, vol. 10, p. 772.
9. B. Meyghani, M.B. Awang, and C.S. Wu: *Materwiss. Werksttech.*, 2020, vol. 51, pp. 550–57.
10. Z.L. Liu, K. Yang, and S.D. Ji: *J. Mater. Eng. Perform.*, 2018, vol. 27, pp. 5605–12.
11. J. Verma, R.V. Taiwade, C. Reddy, and R.K. Khatirkar: *Mater. Manuf. Process.*, 2018, vol. 33, pp. 308–14.
12. Y.S. Sato, S.H.C. Park, M. Michiuchi, and H. Kokawa: *Scripta Mater.*, 2004, vol. 50, pp. 1233–36.
13. A.C. Somasekharan and L.E. Murr: *Magnes. Technol.*, 2004, pp. 31–36.
14. P. Venkateswaran, Z.H. Xu, X. Li, and A.P. Reynolds: *J. Mater. Sci.*, 2009, vol. 44, pp. 4140–47.
15. A. Dorbane, B. Mansoor, G. Ayoub, V.C. Shunmugasamy, and A. Imad: *Mater. Sci. Eng. A*, 2016, vol. 651, pp. 720–33.
16. Y.C. Chen and K. Nakata: *Scripta Mater.*, 2008, vol. 58, pp. 433–36.
17. A. Kostka, R.S. Coelho, J. dos Santos, and A.R. Pyzalla: *Scripta Mater.*, 2009, vol. 60, pp. 953–56.
18. U.F.H. Suhuddin, V. Fischer, and J.F. Dos Santos: *Scripta Mater.*, 2013, vol. 68, pp. 87–90.
19. N. Yamamoto, J. Liao, S. Watanabe, and K. Nakata: *Mater. Trans.*, 2009, vol. 50, pp. 2833–38.
20. Y. Zhao, S. Jiang, S. Yang, Z. Lu, and K. Yan: *Int. J. Adv. Manuf. Technol.*, 2016, vol. 83, pp. 673–79.
21. M. Mofid, A. Abdollah-Zadeh, and F. Ghaini: *Mater. Des.*, 2012, vol. 36, pp. 161–67.
22. S. Ji, R. Huang, X. Meng, L. Zhang, and Y. Huang: *J. Mater. Eng. Perform.*, 2017, vol. 26, pp. 2359–67.
23. H. Liu, Y. Hu, S. Du, and H. Zhao: *J. Manuf. Process.*, 2019, vol. 42, pp. 159–66.
24. X.C. Liu and C.S. Wu: *Mater. Des.*, 2016, vol. 90, pp. 350–58.
25. X.C. Liu and C.S. Wu: *J. Mater. Process. Technol.*, 2015, vol. 225, pp. 32–44.
26. G.K. Padhy, C.S. Wu, S. Gao, and L. Shi: *Mater. Des.*, 2016, vol. 92, pp. 710–23.
27. S. Ji, X. Meng, Z. Liu, R. Huang, and Z. Li: *Mater. Lett.*, 2017, vol. 201, pp. 173–76.
28. X.Q. Lv, C.S. Wu, C.L. Yang, and G.K. Padhy: *J. Mater. Process. Technol.*, 2018, vol. 254, pp. 145–57.
29. S. Kumar, C.S. Wu, Z. Sun, and W. Ding: *Int. J. Adv. Manuf. Technol.*, 2019, vol. 100, pp. 1787–99.
30. S. Kumar and C.S. Wu: *Mater. Today Proc.*, 2018, vol. 5, pp. 18142–51.
31. S. Kumar, C.S. Wu, and G.K. Padhy: *7th Int. Conf. on Welding Science and Engineering (WSE 2017)*, in conjunction with *3rd Int. Symp. on Computer-Aided Welding Engineering (CAWE 2017)*, Shandong University, Jinan, China, 2017, pp. 272–76.
32. Z. Liu, S. Ji, and X. Meng: *Int. J. Adv. Manuf. Technol.*, 2018, vol. 97, pp. 4127–36.
33. B. Strass, G. Wagner, C. Conrad, B. Wolter, S. Benfer, and W. Fürbeth: *Adv. Mater. Res.*, 2014, vols. 966–967, pp. 521–35.
34. B. Langenecker: *Trans. Son. Ultrason.*, 1966, vol. 13, pp. 1–8.
35. Y. Li, S. Tian, C.S. Wu, and M. Tanaka: *J. Manuf. Process.*, 2021, vol. 64, pp. 1412–19.
36. L. Shi, C.S. Wu, and X.C. Liu: *J. Mater. Process. Technol.*, 2015, vol. 222, pp. 91–102.
37. K. Park, G.Y. Kim, and J. Ni: *ASME Int. Mech. Eng. Congr. Expos.*, 2007, vol. 3, pp. 731–37.
38. S. Kumar: *Arch. Civ. Mech. Eng.*, 2016, vol. 16, pp. 473–84.
39. S. Kumar, W. Ding, Z. Sun, and C.S. Wu: *Int. J. Adv. Manuf. Technol.*, 2018, vol. 97, pp. 1269–84.
40. S. Kumar, C.S. Wu, and G. Song: *Metall. Mater. Trans. A*, 2020, vol. 51A, pp. 2863–81.
41. S. Kumar and C.S. Wu: *J. Alloys Compd.*, 2020, vol. 827, art. no. 154343.
42. ASTM International, West Conshohocken, PA, 2008.
43. S. Kumar, C.S. Wu, G.K. Padhy, and W. Ding: *J. Manuf. Process.*, 2017, vol. 26, pp. 295–322.
44. A. Panteli, J.D. Robson, I. Brough, and P.B. Prangnell: *Mater. Sci. Eng. A*, 2012, vol. 556, pp. 31–42.
45. Y. Song, X. Yang, L. Cui, X. Hou, Z. Shen, and Y. Xu: *Mater. Des.*, 2014, vol. 55, pp. 9–18.
46. Y. Wei, J. Li, J. Xiong, F. Huang, and F. Zhang: *Mater. Des.*, 2012, vol. 33, pp. 111–14.

47. L. Peng, L. Yajiang, G. Haoran, and W. Juan: *Mater. Lett.*, 2005, vol. 59, pp. 2001–05.
48. L. Shi, C.S. Wu, S. Gao, and G.K. Padhy: *Scripta Mater.*, 2016, vol. 119, pp. 21–26.
49. J. Zhao, C.S. Wu, and H. Su: *J. Manuf. Process.*, 2021, vol. 62, pp. 388–402.
50. A. Gerlich, P. Su, M. Yamamoto, and T.H. North: *Sci. Technol. Weld. Join.*, 2008, vol. 13, pp. 254–64.
51. J. Mohammadi, Y. Behnamian, A. Mostafaei, H. Izadi, T. Saeid, A.H. Kokabi, and A.P. Gerlich: *Mater. Charact.*, 2015, vol. 101, pp. 189–207.
52. J. Wang, Q. Sun, L. Wu, Y. Liu, J. Teng, and J. Feng: *J. Mater. Process. Technol.*, 2017, pp. 185–97.
53. S.Y. Tarasov, V.E. Rubtsov, S.V. Fortuna, A.A. Eliseev, A.V. Chumaevsky, T.A. Kalashnikova, and E.A. Kolubaev: *Weld. World*, 2017, vol. 61, pp. 679–90.
54. S. Kumar, C.S. Wu, and L. Shi: *Metall. Mater. Trans. A*, 2020, vol. 51A, pp. 5725–42.
55. V. Firouzdor and S. Kou: *Weld. J.*, 2009, vol. 88, pp. 213–24.
56. R. Nandan, T. DebRoy, and H.K.D.H. Bhadeshia: *Progr. Mater. Sci.*, 2008, vol. 53, pp. 980–1023.
57. K. Kumar, S.V. Kailas, and T.S. Srivatsan: *Mater. Manuf. Process.*, 2011, vol. 26, pp. 915–21.
58. A.C. Somasekharan and L.E. Murr: *J. Mater. Sci.*, 2006, vol. 41, pp. 5365–70.
59. S. Ji, S. Niu, J. Liu, and X. Meng: *J. Mater. Process. Technol.*, 2019, vol. 35, pp. 1712–18.
60. A. Kostka, R.S. Coelho, J. dos Santos, and A.R. Pyzalla: *Scripta Mater.*, 2009, vol. 60, pp. 953–56.
61. S. Ji, Z. Li, L. Zhang, Z. Zhou, and P. Chai: *Mater. Des.*, 2016, vol. 103, pp. 160–70.
62. X.C. Liu, C.S. Wu, and G.K. Padhy: *Sci. Technol. Weld. Join.*, 2015, vol. 20, pp. 345–52.
63. D. Dietrich, D. Nickel, M. Krause, T. Lampke, M.P. Coleman, and V. Randle: *J. Mater. Sci.*, 2011, vol. 46, pp. 357–64.
64. J. Mohammadi, Y. Behnamian, A. Mostafaei, and A.P. Gerlich: *Mater. Des.*, 2015, vol. 75, pp. 95–112.
65. B.S. Naik, D.L. Chen, X. Cao, and P. Wanjara: *Metall. Mater. Trans. A*, 2014, vol. 45A, pp. 4333–49.
66. V. Firouzdor and S. Kou: *Metall. Mater. Trans. A*, 2010, vol. 41A, pp. 3238–51.
67. C. Zhou, X. Yang, and G. Luan: *Mater. Chem. Phys.*, 2006, vol. 98, pp. 285–90.

Publisher's Note Springer Nature remains neutral with regard to jurisdictional claims in published maps and institutional affiliations.